New Journal of Physics
The open access journal at the forefront of physics

Deutsche Physikalische Gesellschaft DPG IOP Institute of Physics

High-resolution hard-x-ray photoelectron diffraction in a momentum microscope—the model case of graphite

To cite this article: O Fedchenko *et al* 2019 *New J. Phys.* **21** 113031

IOP Publishing New J. Phys. 21 (2019) 113031 https://doi.org/10.1088/1367-2630/ab51fe

New Journal of Physics
The open access journal at the forefront of physics

Deutsche Physikalische Gesellschaft DPG
IOP Institute of Physics
Published in partnership with: Deutsche Physikalische Gesellschaft and the Institute of Physics

CrossMark

OPEN ACCESS

RECEIVED
14 August 2019

REVISED
9 October 2019

ACCEPTED FOR PUBLICATION
28 October 2019

PUBLISHED
14 November 2019

PAPER

High-resolution hard-x-ray photoelectron diffraction in a momentum microscope—the model case of graphite

O Fedchenko[1,5,6], A Winkelmann[2,6], K Medjanik[1], S Babenkov[1], D Vasilyev[1], S Chernov[1], C Schlueter[3], A Gloskovskii[3], Yu Matveyev[3], W Drube[3], B Schönhense[4], H J Elmers[1] and G Schönhense[1]

[1] Institut für Physik, Johannes Gutenberg-Universität, Mainz, Germany
[2] Laser Zentrum Hannover e.V, Hannover, Germany
[3] Deutsches Elektronen-Synchrotron DESY, Hamburg, Germany
[4] Dept. of Bioengineering, Imperial College, London, United Kingdom
[5] Author to whom any correspondence should be addressed.
[6] Authors contributed equally to this paper.

E-mail: ofedchen@uni-mainz.de

Keywords: photoemission, hard x-rays, photoelectron diffraction, graphite, time-of-flight (ToF) momentum microscopy

Supplementary material for this article is available online

Abstract

Hard x-ray photoelectron diffraction (hXPD) patterns recorded with a momentum microscope with high k-resolution (0.025 Å^{-1} equivalent to an angular resolution of 0.034° at 7 keV) reveal unprecedented rich fine structure. We have studied hXPD of the C 1s core level in the prototypical low-Z material Graphite at 20 photon energies between 2.8 and 7.3 keV. Sharp bright and dark lines shift with energy; regions of Kikuchi band crossings near zone axis exhibit a filigree structure which varies rapidly with energy. Calculations based on the Bloch wave approach to electron diffraction from lattice planes show excellent agreement with the experimental results throughout the entire energy range. The main Kikuchi bands in the [001] zone axis appear fixed on the momentum scale with a width of the corresponding reciprocal lattice vector, allowing to reconstruct the size of the projected Brillouin zone. The newly developed high-energy k-microscope allows full-field imaging of (k_x, k_y)-distributions in large k-fields (up to $>22\ \text{Å}^{-1}$ dia.) and time-of-flight energy recording.

1. Introduction

Launched by the pioneering work of Siegbahn, Fadley and others in the early 1970s [1, 2], x-ray photoelectron diffraction (XPD) has developed into a powerful method to gain information about the geometrical structure of the photo-emitting atomic layers, surface reconstruction and relaxation, as well as adsorbate geometries. The dynamic development of XPD over time is summarised in a sequence of excellent overviews [3–10]. More recently, the method was extended to the hard x-ray range ([11] and references therein); a comprehensive overview of hard x-ray photoemission in general is given in [12].

Core-level XPD is the result of a localised excitation at a given atomic site and the scattering of the resulting photoelectrons of neighbouring atoms. In early observations on single crystal surfaces, the angular distributions were interpreted as being caused by reflection of the photoelectrons on lattice planes of the three-dimensionally periodic bulk crystal [1, 2, 13]. A two-beam dynamical theory was applied to explain the azimuthal variations of photoelectron intensities for single-crystal copper [14, 15]. However, at lower typical XPS energies of <1.5 keV, short-range order scattering in a cluster has become the dominant mode of analysing XPD data, e.g. [16]. The intensity variations, dominated by Kikuchi bands and single-atom forward scattering can be well reproduced using these models, but the two models are consistent with one another if fully converged [7]. As energy increases, the scattering becomes more forward peaked as a result of forward scattering at rows of atoms seen at typical energies of 1 keV. Cluster approaches [15, 16] have proven to reproduce the experimental diffraction patterns with good agreement for cluster sizes as small as few nm. A quantitative comparison [7] between the

XPD cluster picture and dynamical electron scattering from lattice planes showed that the latter is more appropriate for very high energies. Hence, for the present study of hard x-ray photoelectron diffraction (hXPD) the dynamical scattering approach for bulk crystals is expected to be the more efficient theoretical description. By exploiting exchange scattering and multiplet splittings, even antiferromagnetic short-range order has been probed by XPD [17, 18].

Experimentally, XPD is studied using angular-resolved photoelectron spectroscopy. Large polar angular ranges of typically 0°–60° can be observed, mostly by rotating the sample about its surface normal (e.g. [8, 10, 11]). But also display-type electron analysers were developed [19–21] which give direct 2D full-field angular distributions in a wide angular range [22–25]. One main emphasis was to observe the pronounced forward scattering along atom rows in off-normal directions [4, 8], hence the trend to observe a maximum polar angular range. Typical angular resolutions in both angular-scanning and display-type recording modes are $\sim 1^\circ$, but in some cases higher resolutions ($< 1^\circ$ FWHM) have been reached [26–28].

Here we present the first study of XPD using the new technique of momentum microscopy. In this type of photoelectron analyser, a cathode-lens (usually with an electrostatic extractor field) yields a reciprocal image in its backfocal plane (BFP), which is magnified on the image detector. This recording mode bears several essential differences in comparison with previous approaches: The diffractograms are observed in reciprocal space (i.e. on a momentum scale) instead of real-space polar coordinates. The k-field of view in the present study is up to ~ 14 Å^{-1} at 7 keV, corresponding to a small polar angular range of 0°–9°. The k-resolution of ~ 0.03 Å^{-1} corresponds to an angular resolution of 0.03°. For the small angular range, full-field imaging works without sample rotation, similar to the display-type solutions. Larger off-normal observation angles are accessible by rotation of the sample using a mode with zero extractor field. The real-space observation mode (PEEM mode) facilitates checking of surface quality and easy selection of desired sample areas.

The aim of this first detailed momentum-microscopy XPD study was to explore the so far inaccessible regime of high-resolution, small-angle hXPD and to compare the measured diffractograms with state-of-the-art dynamical calculations using the Bloch-wave approach [7, 29]. We stress the complementarity of the present results with XPD work on much larger angular scales. High-resolution k-space mapping offers an increased sensitivity to the effects of long-range order, which can be revealed in the fine structure of bulk diffraction features. Wide-angular-range investigations are focussed on the local order around the photoemitter sites (even without long-range order), as manifested e.g. by the forward-focussing directions toward neighbour sites.

2. Photoelectron diffraction in the Kikuchi model

At kinetic energies in the range of several keV, the probing volume of hard x-ray photoemission is characteristic for the bulk structure of the sample, with severely reduced sensitivity to surface effects. This is why at high kinetic energies photoelectron diffraction effects in single crystals can be interpreted in terms of diffraction effects at the lattice planes of the crystal [1, 14].

Photoelectron diffraction is a special case of the general problem of electron emission from sources inside a crystal for which a general description can be given using the dynamical theory of electron diffraction [13, 30]. Just like in the diffraction of an incident plane wave beam, the geometrical key concept of diffraction patterns from internal sources is the Bragg reflection condition for the crystal lattice. For a specific lattice plane, the Bragg reflection condition with Bragg angle ϑ_{B} is fulfilled for incident and reflected wave vectors on cones with half opening angle of $90^\circ - \vartheta_{\mathrm{B}}$, with the lattice plane normal as the symmetry axis of these so called 'Kossel cones' [13]. Depending on the geometrical conditions of the measurement, the Kossel cones are imaged as conic sections. In the gnomonic projection corresponding to projection from a point source onto a detection plane, for example, the Kossel cones result in hyperbolic edges of the Kikuchi bands. With small Bragg angles and correspondingly large opening angles of the two Kossel cones on either side of a lattice plane, these hyperbolas will look almost linear. When measuring energy-dependent diffraction features in k_x,k_y-space, Kikuchi bands with their lattice plane normals (hkl) in the projection plane will show a constant width corresponding to the reciprocal lattice vectors $\boldsymbol{g}_{hkl}$. Kikuchi bands of inclined planes will vary according to the respective z-component of the $\boldsymbol{g}_{hkl}$ in the projection k-space.

Figure 1 shows an example Kikuchi pattern calculated for Graphite when projected on a planar screen perpendicular to [001]. In figure 1, we look edge-on onto the lattice planes which contain the [001] direction in the centre. These planes are perpendicular to the (001) surface plane. The advantage of the gnomonic projection is the fact that the projections of *all* (!) lattice planes are straight lines, and the intersection of these lines mark a corresponding zone axis, i.e. the direction that is contained by both planes. As can be seen in the inset showing the graphite crystal structure, the (100) and (110) lattice planes correspond to Kikuchi bands at angles of 30°. Similarly, the width of these Kikuchi bands is determined by the lattice plane spacings $d_{hkl} = 2\pi/\boldsymbol{g}_{hkl}$. From a calculation of the structure factors [31], the strongest Kikuchi bands can be expected for the reflections in the

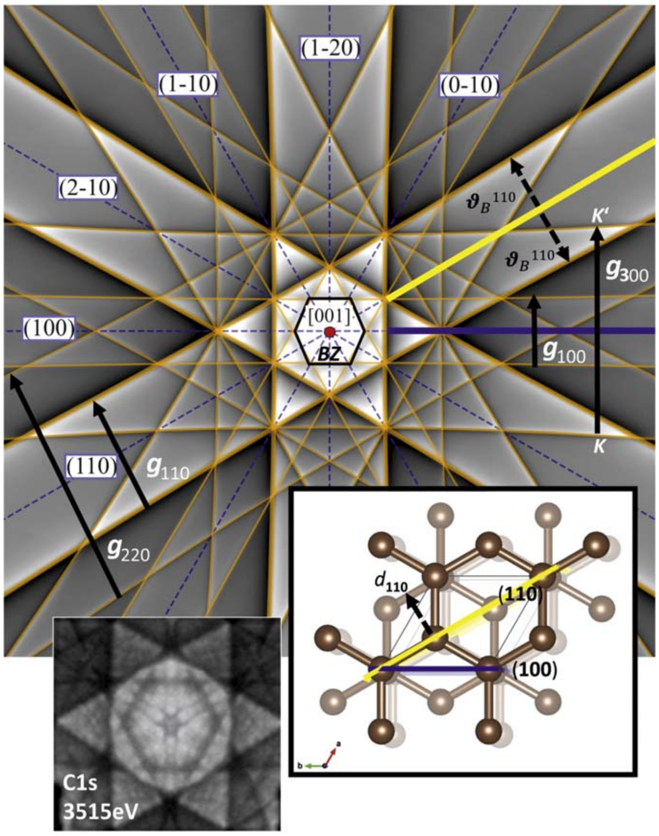

Figure 1. Theoretical Kikuchi pattern of Graphite near the [001] zone axis. Gnomonic projection in a plane perpendicular to [001] with viewing angles ±45°. The blue dashed lines indicate the projections of lattice planes (*hkl*) shown by blue labels. The Kikuchi bands extend from the lattice plane projections by ± the Bragg angle ϑ_B of the reciprocal respective lattice vectors. In the chosen projection of the lattice planes with $l = 0$, the angles between the Kikuchi bands directly correspond to angles between lattice planes in the crystal structure (bottom right inset). The Kikuchi band edges K and K' mark directions on the two Kossel cones with their symmetry axis along $\boldsymbol{g}_{hkl}$, and the angle between the band edges is $2\vartheta_B$. In the k_x–k_y-projection measured in the momentum microscope (bottom left), the size of the Brillouin zone in the projection plane can be calibrated from the width and orientation of the Kikuchi bands related to $|\boldsymbol{g}_{hkl}|$ (inner dark hexagon in bottom left inset is the projected BZ). In the experiment, for the small angular range of <20° relative to [001], the geometry of the gnomonic projection and the k_x–k_y-plane is the same.

order (110), (100), (300), (220) and their symmetry-equivalent reflections, which are considered in the intensity simulation of figure 1 (see below for the theoretical details). The respective Bragg angles ϑ_B can be measured approximately by the angular separation of the Kikuchi band edges from the projection of the lattice planes (*hkl*) shown as dashed blue lines in the band centres. In figure 1, the hyperbolic shape of the Kikuchi band edges is caused by the conic section of the projection plane with the Kossel cones with their symmetry axis along $\boldsymbol{g}_{hkl}$, i.e. we see the Kossel cones edge-on because the selected $\boldsymbol{g}_{hkl}$ with $l = 0$ are lying in the projection plane. This property also makes it possible to measure the lengths $|\boldsymbol{g}_{hkl}|$ of the reciprocal lattice vectors in the experimental pattern measured as a projection in the k_x–k_y-plane in the momentum microscope. If the corresponding low-order bands can be determined in the experiment, this allows to measure the outline of the two-dimensional Brillouin zone in the projection plane as marked by BZ in figure 1.

Concerning the quantitative simulation of the electron diffraction effects from atomic emitters, the Bloch wave model [32] is an efficient approach for simulations of photoelectron diffraction in the hard x-ray regime. Most importantly, the three-dimensional symmetry of the atomic arrangements around the photoemitters is explicitly included in the theoretical formulation. This is a simplification compared to multiple scattering cluster models, which allow arbitrary atomic arrangements to be handled, including surface effects. In the limit of bulk diffraction in single crystals, however, both types approaches deliver similar results [7, 29].

In brief, the Bloch wave model of high-energy electron diffraction considers the coherent scattering of an incoming plane wave beam by the crystal, which leads to a spatially modulated probability to find an electron at a specific point in the crystal unit cell. Application of the reciprocity principle [33] shows that this is equivalent to the time-reversed problem of calculating the intensity that is originating at a specific point in the unit cell and which is then diffracted into a plane wave that moves into a direction measured by the electron energy analyser. In the Bloch wave approach of the dynamical theory of electron diffraction in single crystals [34] the scattering potential is assumed to have the bulk symmetry, and the wave function $\Psi(\boldsymbol{r})$ inside the crystal is described as a superposition of j Bloch waves:

$$\Psi(r) = \sum_j c_j \exp[\mathrm{i}\boldsymbol{k}^{(j)} \cdot r] \sum_g C_g^{(j)} \exp[\mathrm{i}\boldsymbol{g} \cdot r] \tag{1}$$

with wave vectors $\boldsymbol{k}^{(j)}$ and the reciprocal lattice vectors g. For a given incident beam with kinetic energy E, the Schrödinger equation is then solved for the expansion coefficients c_j and $C_{\boldsymbol{g}}^{(j)}$, as well as the wave vectors $\boldsymbol{k}^{(j)}$ of the Bloch waves. The calculation of the $\boldsymbol{k}^{(j)}$ for a given energy E can also be called the 'inverse band-structure problem' [35], because in electronic band-structure calculations, the energy levels E_j in a band j are determined for a given Bloch wave vector $\boldsymbol{k}$. For high-energy electron diffraction, the Schrödinger equation can be transformed into an eigenvalue problem for a general complex matrix by introducing the high-energy forward-scattering approximation [36]. The eigenvalue problem is solved by standard numerical procedures, where the matrix dimensions are determined by the number of the Fourier coefficients $\boldsymbol{V}_{\boldsymbol{g}}$, which are used to approximate the periodic scattering potential. These coefficients are related to the respective reciprocal space vectors or reflecting sets of lattice planes $\boldsymbol{g}_{hkl}$. Since we measure core-level photoelectrons, we know that these electrons are produced at the positions of the crystal atoms. We thus calculate the respective overlaps of the diffracted wave function with point sources centred at the positions of the emitter atoms, broadened by thermal vibrations [32]. Considering low-energy photoemission and electron diffraction, a more general Bloch wave band-structure approach can be used to describe, for example, angle-resolved photoemission from valence bands [35].

One of the advantages of the Bloch wave approach is that reciprocal lattice vectors related to individual lattice planes are used to describe the effects of crystal symmetry. This allows a rather direct connection between the underlying building blocks of the theory, which are the Fourier coefficients of the crystal potential, and the experimentally observed Kikuchi band features, which are related to the projections of the lattice planes. In comparison, the real-space cluster approach is extremely effective at describing the local short-range order around an emitter or scatterer and allows to interpret the diffraction pattern in terms of changes in the nearest emitter environment because the individual scatterer potentials are the building blocks of the cluster approach. Such short-range effects, which break the long-range symmetry, are hard to handle in the Bloch wave approach for a bulk single crystal. On the other hand, the Bloch wave approach is very efficient for handling the connection of diffraction and internal inelastic excitations of the crystal, because the transition matrix elements can be formulated in a straightforward way based on plane-wave expansions of states, which are defined with well-defined crystal momentum $\boldsymbol{k}$ from the outset.

3. Experimental and theoretical details

3.1. Experimental technique

Hard x-ray XPD patterns were taken in the geometry sketched in figure 2 for 20 different photon energies in the range of 2.840–7.283 keV. The signal from the C 1s core level was selected by setting the proper sample bias such that the point of best focussing coincides with the maximum of the C 1s peak (see spectrum in figure 2). Graphite turned out to be favourable as the first example of Kikuchi-band observation using the new method. C 1s is the only core level; hence its signal appears prominent above a very low background. Moreover, due to its low Z the scattering factor is low [36] which leads to pronounced Kikuchi patterns with straight lines and bands clearly visible in real time (exposure 1 s) which makes adjustment of the optics very easy. We used a natural Graphite single crystal (origin: Ticonderoga mine, USA).

The experiment was carried out at the high-brilliance beamline P22 of PETRA III at DESY (Hamburg) providing up to 1.1×10^{13} hard x-ray photons per second in a focal spot of $\sim 20 \times 15\ \mu\mathrm{m}^2$ [37]. For most measurements we used the Si(111) double crystal monochromator ($\Delta E/E \sim 1.3 \times 10^{-4}$, bandwidth 450 meV at $h\nu = 5$ keV), a few measurements were done with the Si(311) crystal ($\Delta E/E \sim 3 \times 10^{-5}$, flux $\sim 2 \times 10^{12}\ h\nu/s$, bandwidth 155 meV at 5 keV). A bandwidth of ~50 meV is already available using a single Si(333) channel-cut crystal operating close to 6 keV [38]. A similar small bandwidth will be possible in the full energy range using an additional post-monochromator.

The present results have been obtained with a new design of time-of-flight (ToF) momentum microscope. The operation principle is the same as described in [39] but its electron optics has been optimised for maximum k-field acceptance. The key element is the objective lens, which can image diameters exceeding 22 Å^{-1} with low aberration and image field distortion in the Fourier image in the BFP (figure 2). The subsequent ZOOM optics transfers this high-energy image to the low drift energy in the field-free drift tube (length 1 m) with well-shielded magnetic fields. Typical drift energies for sufficient energy/time dispersion in HAXPES experiments are in the range of 20–50 eV. The large transversal electron momentum causes a substantial angular divergence in the drift section. The electrons are recorded with respect to their (x, y, t)-coordinates by a delay-line detector [40] with 80 mm active diameter having 80 μm and 180 ps lateral and time resolution, respectively. For the present

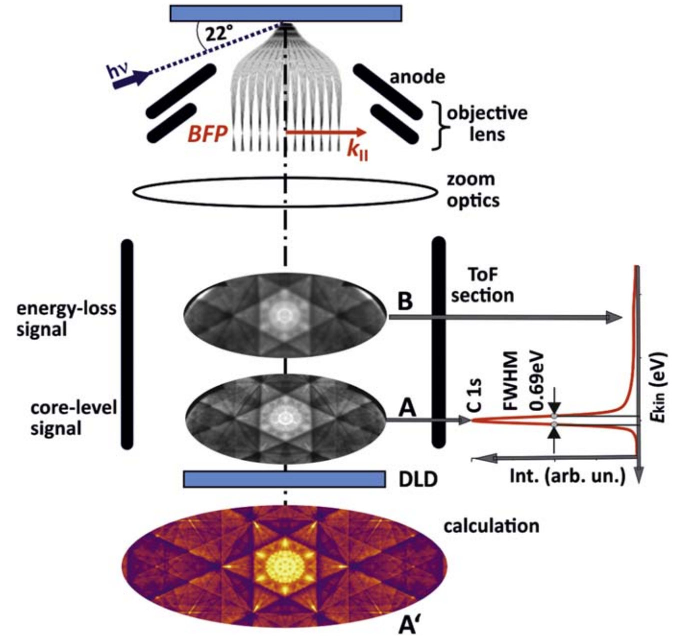

Figure 2. Schematic view (strongly simplified) of the time-of-flight momentum microscope and recording scheme of core-level hard x-ray photoelectron diffraction (hXPD). The basic principle is the same as in all cathode-lens *k*-microscopes, i.e. a momentum image exists in the backfocal plane BFP of the objective lens and this *k*-image is magnified on the image detector. Energy discrimination is facilitated by a low-energy ToF section which converts the energy distribution to a time spectrum. This time spectrum is recorded by a delay-line detector (DLD). *A* and *B* are recorded diffractograms at the carbon 1s peak and in the inelastic-loss part of the spectrum (at $E_{\mathrm{final}} = 7.015$ and 7.006 keV, respectively) as denoted by the arrows. A' shows the calculated hXPD pattern corresponding to measurement *A*. In the present instrument the diameter of the imaged *k*-field can be zoomed between ~2 $Å^{-1}$ and > 22 $Å^{-1}$.

geometry maximum *k*-fields of 14–16 $Å^{-1}$ are recorded, limited by the 80 mm diameter of the detector. For valence-band *k*-mapping this covers the central Brillouin zone (BZ) and two rings of repeated BZs (in total 19 BZs in parallel for the hcp metal Re [38]).

At this point, it is worthwhile considering which *k*-field-of-view is adequate for recording detail-rich hXPD patterns. Compared to the previous investigations which focussed on the local order around the photoemitter sites (as manifested e.g. by the forward-focussing directions toward neighbour sites), high-resolution *k*-space mapping offers an increased sensitivity to the effects of long range order, which can be revealed in the fine structure of bulk diffraction features. A *k*-microscope observes XPD patterns in coordinates of the parallel momentum $k_{||}$. Their interpretation and discussion relies on *k*-space coordinates as well (see below). It is well known that in the several-keV range *Kikuchi bands* dominate the photoelectron diffractograms [7]. Kikuchi diffraction [41] has been studied in much detail in scanning and transmission electron microscopy [42, 43], where it is an established method for structural microanalysis. In the present work we studied the inner region of the hXPD pattern, which looks practically structureless in most previous XPD studies, see, e.g. the patterns recorded with hard x-rays at comparable energies (5.4 keV) in [11]. The measured *k*-image of the C 1s core-level (signal *A*) in figure 2 shows a pronounced Kikuchi pattern with rich fine structure. The result of the Bloch-wave calculation (A') is in perfect agreement with experiment.

The *k*-space metric of Kikuchi bands crossing the centre of the XPD pattern of a low-index crystal surface is simple and allows reconstructing the projected reciprocal lattice. As described in figure 1 the central bands originate from sets of lattice planes oriented perpendicular to the surface. In the case of graphite the dominating sixfold-symmetric Kikuchi pattern (*A* and A' in figure 2) originates from reflection at the lattice plane (110), see figure 1. The width of the prominent Kikuchi band is given by the corresponding reciprocal lattice vector $|\boldsymbol{g}_{110}| = 2\pi/1.228$ Å $= 5.1166$ $Å^{-1}$. In order to see the central crossing region and its surroundings in much detail, an imaged *k*-field diameter of about two times the bandwidth, i.e. ~10 $Å^{-1}$ should be sufficient. The electron optics resolves approx. 400 pixels along the image diagonal, corresponding to a *k*-resolution of 0.025 $Å^{-1}$. Translated to polar coordinates this value corresponds to an angular resolution of 0.034° (for 7 keV energy). We recall that the hXPD patterns have a fixed metric in *k*-space (fixed width of the Kikuchi bands) and due to the high momentum resolution the rich fine structure in the crossing region can be resolved. This high resolution comes at the expense of the size of the *k*-field. Diameters above 2 times the width of the Kikuchi band are sufficient for a detailed comparison with a calculated hXPD pattern (compare *A* and A').

Parallel energy recording via ToF yields energy bands of several eV width in parallel in a single acquisition. Hence, it is possible to extract several different diffractograms from a single 3D data array, as demonstrated in

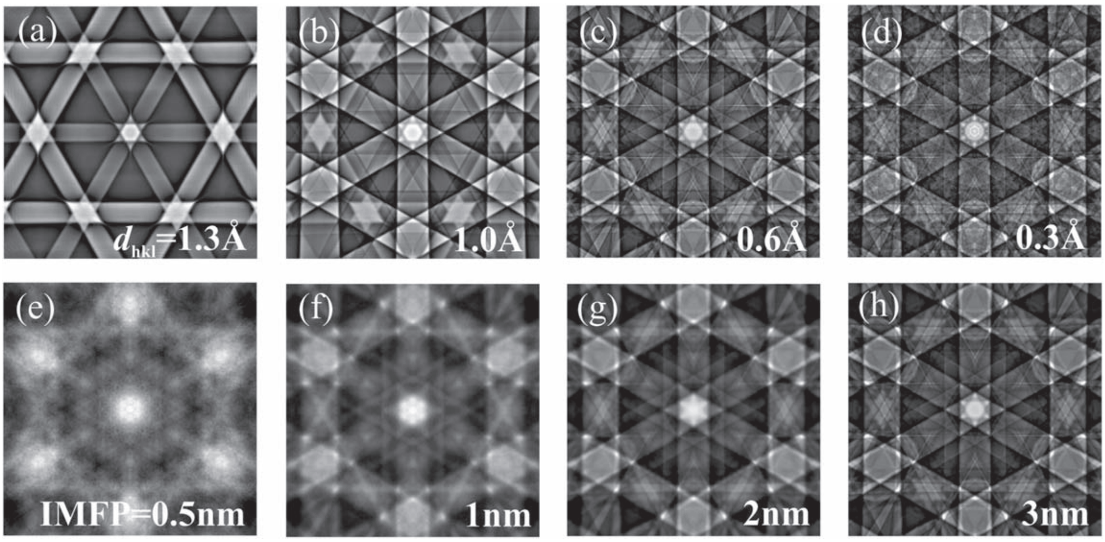

Figure 3. Model calculation for Graphite at 7.015 keV kinetic energy, showing the influence of the number of considered lattice planes (a)–(d) and inelastic mean free path (IMFP) (e)–(h) on the development of Kikuchi features. The limits of the gnomonic projection are at ± 45° from the central [001] zone axis. (a)–(d) The minimum lattice plane distance d_{hkl}, is indicated below each simulation. The inelastic mean free path was fixed to 9 nm. (e)–(h) The IMFP is indicated below each simulation. The minimum lattice spacing d_{hkl} is 0.6 Å.

the lower part of figure 2. Integrating over a small energy interval close to the maximum of the C 1s signal (here at a kinetic energy of 7.015 keV) yields the core-level diffractogram (*A*). Integrating over an energy interval in the low-energy tail (here around a loss-energy of 8 eV) yields the 'energy-loss hXPD diffractogram' of the electrons that have been inelastically scattered (*B*). In the present case the diffractogram of the scattered electrons looks very similar to the C 1s diffractogram. This is different for compounds with several constituent atoms on different sites. The width of the usable energy interval is determined by the chromatic aberration of the lens optics, which depends on the size of the photon footprint on the sample surface. Given the footprint of $20 \times 30\ \mu\text{m}^2$ in the present experiments, the usable interval is up to ~8 eV.

All results shown below have been obtained with a moderate extractor field of the order of 500 V mm^{-1}. The new objective lens allows operation at zero extractor field, thereby sacrificing about 20% of the size of the *k*-field. The zero-field mode opens the path to strongly off-normal emission, in principle until grazing takeoff angle. So, if certain angular intervals are particularly sensitive on structural changes, e.g. in phase transitions, these intervals can be selected using zero-field mode and off-normal emission [38]. An example of such an off-normal hXPD pattern is shown in the supplemental information is available online at stacks.iop.org/NJP/21/113031/mmedia. The size of the momentum-space interval in this mode varies between 12 and 18 Å^{-1} dia., depending on final-state energy.

3.2. Kikuchi diffraction simulations for graphite

The following parameters were used in the simulations discussed below. The lattice constants of Graphite were taken as $a = 2.459$ Å and $c = 6.969$ Å. For description of the observed region in *k*-space, we used a total set of about 3800 possible reciprocal lattice vectors $\boldsymbol{g}_{hkl}$ with lattice spacings $d_{hkl} > 0.1$ Å, from which an average number of about 70 strong reflections was selected for exact matrix diagonalization of the Schrödinger equation at each *k*-vector of observation. The inelastic mean free path (IMFP) was assumed to be 9 nm in the whole energy region between 2.5 and 7 keV. The phenomenological effects of thermal vibrations at the measurement temperature of 30 K during the experiments and other types of remaining disorder were included via a Debye–Waller parameter of $B = 0.2$ Å^2, where B for the reflection $\boldsymbol{g}_{hkl}$ is related to the expression for the kinematic intensity $I(hkl) = f_{hkl}^2 \exp(-2M)$ with $M = B(\sin\theta_{hkl}/\lambda_e)$, taking θ_{hkl} as the Bragg angle and λ_e as the electron wavelength [44].

In order to illustrate the effects of the considered number of lattice planes in the Kikuchi pattern simulation, in figures 3(a)–(d) we show simulations with a decreasing minimum lattice spacing d_{hkl}. It can be seen that the lattice planes with small spacings and correspondingly large Bragg angles are responsible for the formation of the fine structure in the Kikuchi pattern, including the dark features inside the central zone axis. We also note that circular features and other complex intensity distributions are all formed as envelopes of lines.

Figure 3(a) starts with the set of (1 0 0) lattice planes which have the largest spacing of $d_{100} = 2.13$ Å, leading to a very simple hexagonal pattern of crossing Kikuchi bands. The next step (b) includes additionally the set of

(110) with spacing $d_{1-20} = 1.23$ Å, causing a new set of wider Kikuchi bands being rotated by 30° with respect to the narrower (100) bands. The (110) set causes the fundamental strongest bands seen in the experiment, whereas the (100) set appears much weaker as can be expected from a structure factor analysis [31]. As shown in the simplified pattern in figure 1, the strongest bands are expected for the reflections in the order (110), (100), (300), (220) and their symmetry-equivalents. The (110) bands are expected to be almost twice as strong as the (100), which is also seen in the dynamical simulations of figures 3(a) versus (b). Note that the central star of (a) shows up as fine structure in (b)–(d). This is an important principle: near strong zone axis, i.e. inside the crossings of strong Kikuchi bands, the fine structure can be a fingerprint of other sets of Kikuchi bands, which, for example, have a larger d_{hkl} (smaller band width) or which are inclined to the planes of the main feature.

The Kikuchi patterns will also depend on the IMFP, as is shown in figures 2(e)–(h). Due to the reduced multiple scattering in thin crystal regions, the patterns for IMFPs below 5 nm look increasingly blurred for a decreasing IMFP. The Kikuchi patterns of Graphite converge for an IMFP near 9 nm in the energy range between 2.5 and 7 keV that is investigated here. In figure 2(e) the strong confinement of the IMFP to 0.5 nm (less than the lattice constant c) leads to a suppression of the long-range diffraction features. In turn, this pattern somewhat resembles a result of a calculation in the cluster model at low energies. The outer six bright spots in (e) reflect the forward-scattering at nearest neighbours in the next layer (averaged over all sites of the Graphite lattice).

We conclude that the Bloch-wave approach to electron diffraction from lattice planes is very useful to interpret diffraction features of hXPD patterns, which are caused by the bulk crystal structure. From the point of view of quantum mechanics, the Ansatz for the wave function $\Psi(\boldsymbol{r})$ inside the crystal as a superposition of Bloch waves with well-defined wave vectors $\boldsymbol{k}$ and reciprocal lattice vectors g (equation (1)) [34] is a proper description for fast electrons in a bulk crystal and hence adequate for deeply-bulk-sensitive photoemission. We will see that this model yields excellent agreement with the experimental results for Graphite throughout the entire energy range from 2.3 to 7 keV. In particular, we will discuss the fine structure near the [001] zone axis (see section 4.2), which is caused by Bragg reflection of electrons from lattice planes which do not contain the [001] directions. Such bulk effects on very small angular ranges would be extremely hard to handle in a spherical wave cluster approach, because of the necessary requirements on the degree of the spherical harmonics used for the scattering calculation, i.e. the angular frequencies of the spherical harmonics need to fit to the observed angular variations in the measured data.

4. Results and discussion

4.1. Carbon 1s diffractograms

Figure 4 presents a collection of the C 1s core-level measurements at 18 photon energies between 2.8 and 7.3 keV. The whole sequence was measured within a few hours thanks to the parallel acquisition scheme and the high brilliance of beamline P22 at PETRA III. Recording hXPD patterns via full-field k-imaging is an entirely new technique and before we discuss details of the measured patterns it is worthwhile addressing some special properties of k-imaging instruments.

The quantity relevant for the diffraction dynamics is the photoelectron wavelength λ_e inside of the material, related to the final-state momentum $\boldsymbol{k}_{\mathrm{final}}$ as $\lambda_e = 2\pi/|\boldsymbol{k}_{\mathrm{final}}|$. When deriving this quantity from the photon energy set by the monochromator and the tabulated binding energy of C 1s in Graphite ($E_{\mathrm{B}} = 284$ eV), two additional empirical quantities have to be taken into consideration. The effective mass m_{eff} of the high-energy photoelectron can still differ from the free-electron mass m_e. In addition, the final-state energy E_{final} inside of the material is higher than the vacuum kinetic energy E_{kin} by the inner potential V_0^*. The final-state momentum is given by

$$|k_{\mathrm{final}}|/\text{Å}^{-1} = (1/\hbar)\sqrt{(2m_{\mathrm{eff}}E_{\mathrm{final}}/eV)} \approx 0.512\sqrt{(m_{\mathrm{eff}}/m_e)(E_{\mathrm{final}}/(eV)}, \quad E_{\mathrm{final}} = hn - E_{\mathrm{B}} + V_0{}^*, \qquad (2)$$

where both E_{B} and V_0^* are referenced to the Fermi energy and the work function does not show up since we consider the electrons inside of the crystal. V_0^* and m_{eff} are assumed to be energy dependent, i.e. there is no 'universal' final-state parabola that is valid throughout a large energy range. For Graphite we take the value $V_0^* = 13$ eV from [45] and assume $m_{\mathrm{eff}}/m_e = 1$. Measurements for tungsten yielded $m_{\mathrm{eff}}/m_e = 1.07$ at 1 keV [38] and 1 at 6 keV [46]. For Mo we found $m_{\mathrm{eff}}/m_e = 1.03$ at 460 eV and $m_{\mathrm{eff}}/m_e = 1$ already at 1.7 keV [47]. For these reasons, the panels list the final-state energies and not the photon energies.

For a large variation of several keV of the initial kinetic energy in vacuum E_{kin} the k-field of view of the momentum microscope varies substantially. This is a general property of cathode lenses and a consequence of the rather small extractor voltage U_{extr} in relation to the kinetic energy. The deviation from a constant field-of-view scales with the 'immersion ratio' $E_{\mathrm{kin}}/(E_{\mathrm{kin}}+eU_{\mathrm{extr}})$ which varies from 0.23 to 0.58 in the series of figure 4. For comparison, in a typical LEEM experiment this ratio is $< 10^{-3}$, i.e. in LEEM the k-field of view is perfectly achromatic upon variation of the kinetic energy in the eV range [48, 49]. In order to compare diffractograms

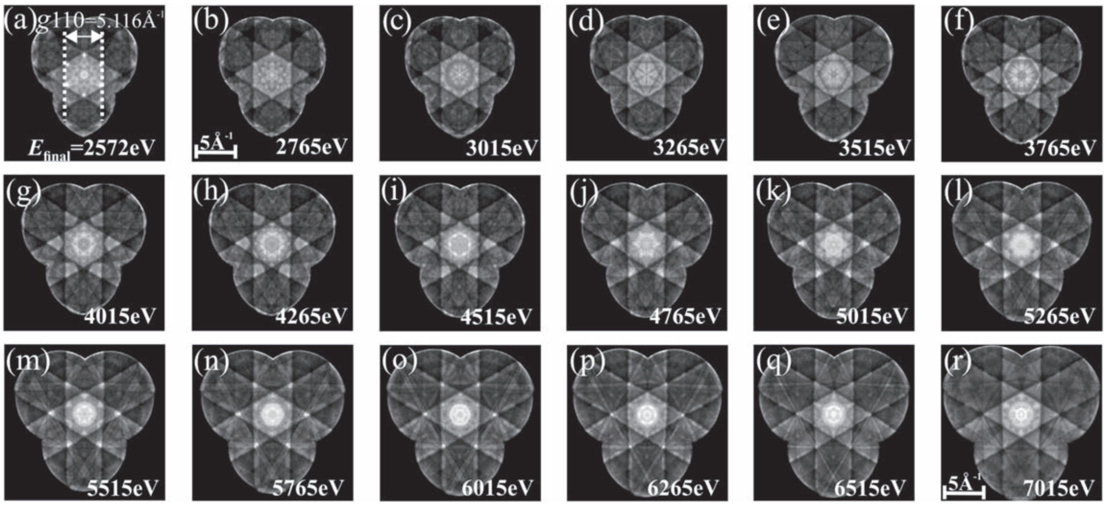

Figure 4. Sequence of measured hard-x-ray photoelectron diffraction (hXPD) patterns of the carbon 1s core level in graphite at photon energies between 2840 and 7283 eV, corresponding to final-state energies given in panels (a)–(r). The width of the prominent Kikuchi band (double arrow in (a)) is given by $|\boldsymbol{g}_{110}| = 5.1166$ Å^{-1}. The k-scale is identical in all panels, i.e. the width of the Kikuchi band stays constant in momentum images, independent on energy. The corresponding angular width of this Kikuchi band varies from 11.8° at $E_{\text{final}} = 2572$ eV (a) to 6.9° at 7015 eV (r).

taken at different kinetic energies with each other and with theory we have scaled all patterns to identical k-scales. Moreover, the patterns have been threefold symmetrized (as described in the supplement).

The eye-catching features in all images are the following.

(i) The bright central hexagon being the zone axis, i.e. the intersection region of all three (110) Kikuchi bands.

(ii) The adjacent triangles being the intersection region of two of the three bands, visible bright in (f).

(iii) The three (110)–bands being confined by a dark line on both sides (best visible at high energies, see (r)).

(iv) The outer tips of the triangles showing a pronounced intensity enhancement between 5 and 6.3 keV, see (k)–(p).

Closer inspection reveals many fine details.

(v) The filigree internal structure of the central hexagon.

(vi) The system of fine dark and bright lines across the entire field of view, and

(vii) Further spot-like intensity enhancements at crossing points of lines (e.g. in (q)).

Features (i)–(iv) are fixed on the k-scale, (iv) appears almost ‘reflex-like’ in (n)–(p). (v)–(vii) are different in all panels (a)–(r), most of the lines (vi) shift with varying energy and the reflex-like spots (vii) show a resonance-like spectral dependence.

At $E_{\text{final}} = 7015$ eV we have $|\boldsymbol{k}_{\text{final}}| = 42.9$ Å^{-1}. The border of the Kikuchi band passes the centre of the pattern ($k_{||} = 0$) at a distance of 2.558 Å^{-1}, which corresponds to a polar angle of only 3.4° in panel (r). This underlines that a very high angular (or momentum) resolution is indispensable in order to observe the narrow lines and the fine structure in the diffractograms.

The sequence reveals the remarkably strong energy variation of the fine structure within the central hexagon. We have seen in figures 1 and 3 that this fine structure is partly connected with the (100)—type Kikuchi bands. At higher energies (bottom row of figure 4) there appear to be rings around the zone axis with diameter resembling the bright central feature in figure 1 with $g_{-100} = 2.95$ Å^{-1}.

In view of previous XPD results in literature the rich structure of fine details in a small angular range of a few degrees and their rapid variation with energy were surprising and rose the incentive to understand the structure of the patterns by means of a diffraction calculation. The second surprise was the excellent one-to-one agreement of the Bloch-wave model calculation with the experiment. Figure 5 shows a selection of five energies, the full sequence is shown as a movie in the Supplemental Material. The figure reveals that, without exception, all details contained in the measured diffractograms are found in the calculation as well. The only significant

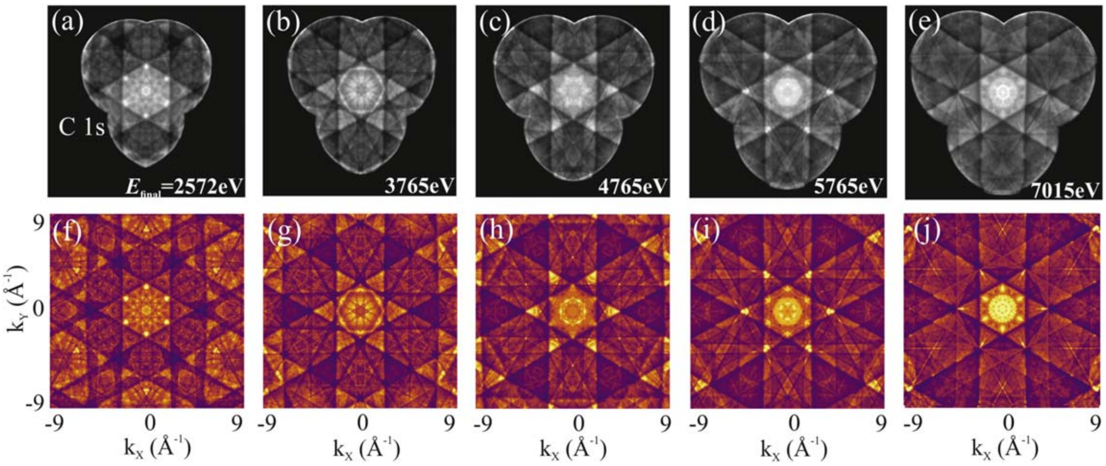

Figure 5. Comparison of measured (a)–(e) and computed (f)–(j) carbon 1s hXPD-patterns of graphite. Close inspection reveals the perfect one-to-one correspondence except for differences in brightness of some details and a larger blur in the experimental patterns. The full sequence is available as movie in the Supplemental Material.

differences are that the experimental patterns are slightly blurred and some details appear at different relative brightness. All above-mentioned features (i)–(vii) appear in theory as well. Compare, e.g. details of the fine-structure in the inner hexagon or the resonance like enhancement at the tips of the triangles in figures 5(d) and (j). In order to probe the agreement at a selected subtle detail we investigate the region close to 3.765 keV in the next section.

4.2. Zone axis fine structure due to inclined lattice planes

A particularly interesting feature appears in the region between 3.0 and 3.5 keV where it seems that narrow Kikuchi bands are running through the centre, changing their contrast at the crossing point 3.265 keV (see figures 6(a)–(c) for the experiment, (d)–(f) for the calculation). The appearance of such narrow bands which also change their width rapidly with energy is not expected from the crystal structure of Graphite, where the narrowest bands are caused by the (100) bands in the [001] zone axis (compare figure 1).

In order to analyse the geometrical situation at the investigated energies, we show in figures 6(g)–(i) the two groups of low-index lattice planes, which are responsible for the formation of the main hexagonal zone axis feature. The group with larger spacing is [(110), (2–10) and (1–20)], the one with narrower spacing [(100), (1–10) and (0–10)]; note that the widths of the corresponding Kikuchi bands reflect the reciprocal lattice. A comparison to the experimental data shows that the angular width of these bands is decreasing with increasing kinetic energy as expected. In addition to these wide bands, in the experiment (a)–(c) we see the narrow band-like features (marked by red lines and arrows), which cross the central [001] direction and result in a feature with higher intensity at 3.015 keV and a dark feature at 3.515 keV. These band-like features are perfectly reproduced by the calculation (d)–(f). The alignment of these features with the projected (110) lattice planes shown as dashed blue lines in figures 6(g)–(i) seemingly indicates a connection between these features and the (110) lattice planes.

This assumption does not need to be true, as can be seen by comparison to the schematic sketch in figures 6(p)–(r). If we consider the Kikuchi bands for the (111)-type planes, the geometrical positions of their band edges at the given kinetic energy agree very well with the features observed in the experiment. The (111)-type lattice planes give rise to so-called *higher order Laue zone* (HOLZ) reflections, which are characterised by a non-zero component of the relevant g-vectors parallel to a specific zone axis. In the present case, this correspond to all *ghkl* which have a non-zero *l*, in contrast to the (*hk*0) reflections in the zero-order Laue zone (ZOLZ) sketched in figures 6(g)–(i). The lattice planes with ghk0 have their normal perpendicular to [001], whereas the (111) planes are inclined at a different angle.

In order to prove our hypothesis about the role of the (111)-related HOLZ reflections, we use hXPD Bloch wave diffraction simulations as shown in figures 6(j)–(o). In the simulations of figures 6(j)–(l) we included only the main 12 reflections of the (100) and (110) types and we then switched on the additional 12 (222)-type reflections in figures 6(m)–(o). It can clearly be seen that the inclusion of these latter reflections (indices given in (q)) leads to the appearance of the features marked in red in figures 6(a)–(c). The effect of $\boldsymbol{g}_{222}$ is relatively strong because the absolute value of the structure factor of the (222) HOLZ reflections is still about 1/3 of the structure factor of the strongest (110) ZOLZ bands.

The calculation in figures 6(m)–(o) and geometrical analysis in (p)–(r) shows that the change from light to dark contrast in the centre is caused by the contraction of Kikuchi bands which correspond to different lattice

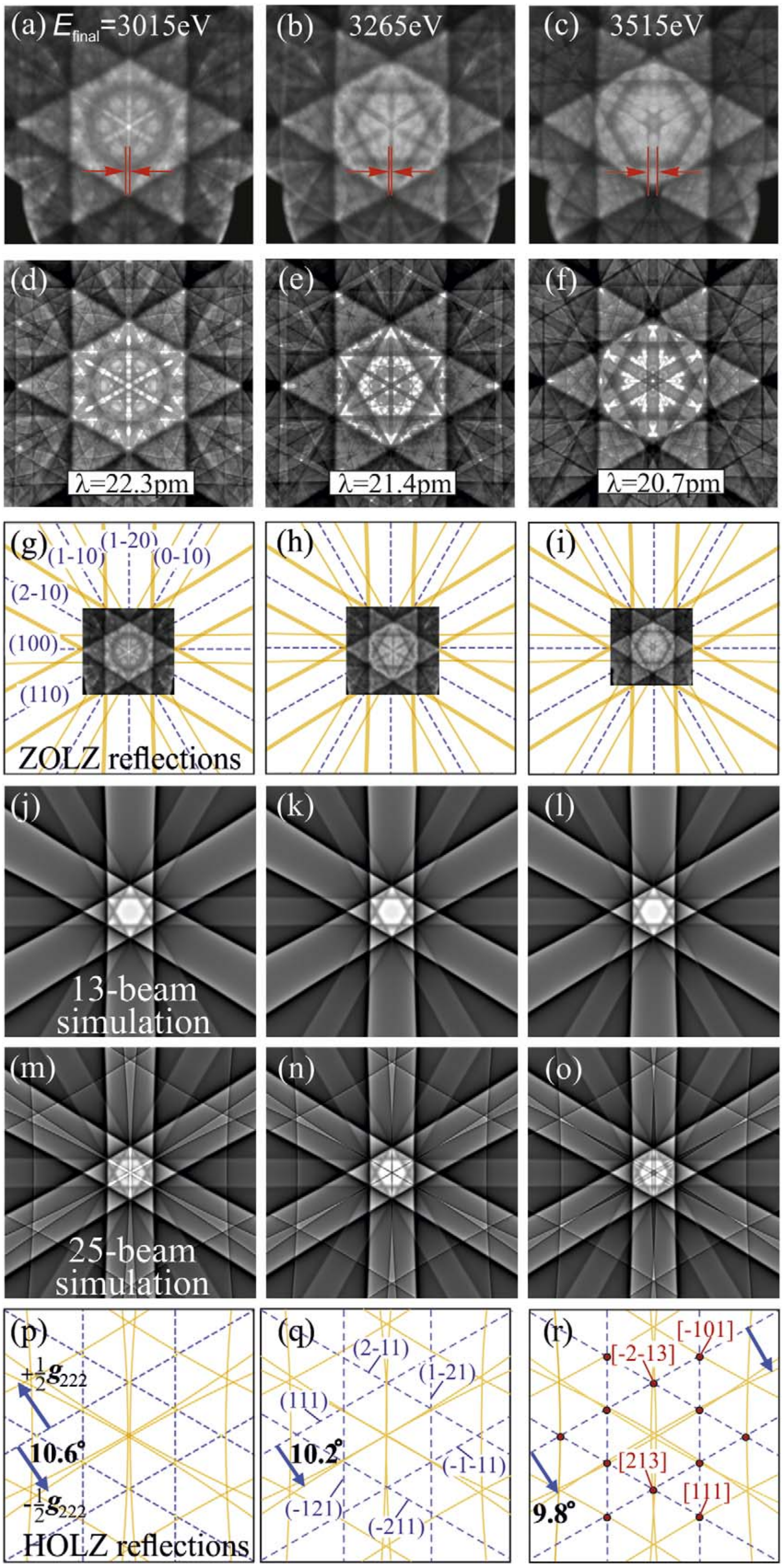

Figure 6. Analysis of the contrast reversal in the crossing region of two HOLZ (higher-order Laue zone) reflections in the vicinity of $E_{\mathrm{final}} = 3265$ eV. (a)–(c) Experimental and (d)–(f) calculated diffractograms in this energy region; red lines and arrows denote the narrow 'band'. (g)–(i) and (p)–(r) Lattice planes labelled (*hkl*) (blue dashed lines) in the zero-order Laue zone (ZOLZ) and higher-order Laue zone (HOLZ), respectively. The latter are responsible for the change of the features in the centre of the measured area. The lattice planes in (p)–(r) are inclined towards the surface, and the reflections correspond to {222} with $d_{222} = 1.014$ Å and corresponding Bragg angles near 10°. The change of the features near the central [001] zone axis is caused by the change in Bragg angles from 10.64° (3015 eV), 10.22° (3265 eV), to 9.84° (3515 eV). (j)–(l) and (m)–(o) Result of a 13- and 25-beam simulation, respectively.

planes, i.e. the band edges seen in the centre do not correspond to $\boldsymbol{g}_{hkl}$ and $\boldsymbol{g}_{-h-k-l}$ for the same h, k, l. Instead, at the lower energy of 3.015 keV, the light region is contained inside two different overlapping Kikuchi bands with a Bragg angle of 10.6°, while at the higher energy of 3.515 eV the Bragg angle is only 9.8° and the regions are now slightly outside of both Kikuchi bands, so that the low-intensity part of the Kikuchi edge profile is causing the appearance of the dark features. One edge of the full Kikuchi band is ~20° away from the other. We also note that in addition to the [001] direction which marks the hexagonal symmetry axis, additional lattice directions [*uvw*] can be derived as crossing points of the HOLZ lines as shown in figure 6(r). However, these lattice directions do not correspond to any easily observable features.

In summary of figure 6, we have illustrated the efficacy of the lattice plane interpretation for features in hXPD patterns. A crystallographic interpretation, of course, is also possible with diffraction simulations carried out in a cluster approach. The key advantage of the Bloch wave approach is, however, that the experimentally observed crystallographic features of lattice planes have one-to-one representatives in the theory (i.e. the Fourier coefficients of the scattering potential). In a practical analysis, this means that we can selectively switch on or off some specific lattice planes of interest as shown in figures 6(j)–(o). This would hardly be possible in a cluster approach, in which the concept of 'lattice plane' does not appear in the theoretical formulation. Instead, the cluster approach excels in a similar manner at explaining features, which are caused by scattering at atomic dimers etc, where the Bloch wave approach requires considerable effort [29].

5. Summary and conclusions

This paper presents the first photoelectron diffraction study with a momentum microscope at photon energies in the hard x-ray range. We have chosen a Graphite single crystal because it is prototypical for an elemental material with low scattering factor. The diffraction patterns recorded at 18 different photon energies between 2.5 and 7.3 keV (beamline P22, PETRA III, DESY, Hamburg) are dominated by the principal Kikuchi bands, originating from Bragg reflection at the (110)-set of lattice planes. The crossing region near the [001] zone axis of the sixfold-symmetric (110) Kikuchi bands exhibits a rich fine structure, which is partly originating from lattice planes that are inclined relative to the main (110) planes.

For interpreting the experimental results, we performed a series of calculations of Graphite diffraction patterns at identical kinetic energies using the Bloch-wave approach to electron diffraction from lattice planes. Making direct use of the translational symmetry of crystals, this model is expected to be more efficient at high photoelectron energies than the more common cluster-type calculations. One central question was at which minimum energy the Bloch-wave model is capable of describing the experimental diffractograms. Alongside with the experimental discovery of a filigree fine structure of the measured diffractograms, a similarly surprising result is the excellent one-to-one agreement of the Bloch-wave calculations with the experimental diffraction patterns throughout the entire energy range down to the lowest energy accessible at beamline P22.

The Bloch wave simulations were used to show that the (222) Bragg reflections govern the fine structure inside the [001] zone axis, despite the fact that these (222)-type Kikuchi bands are otherwise less visible due to their lower structure factor. The analysis explained a contrast reversal in the crossing region of two HOLZ (higher-order Laue zone) reflections in the vicinity of $E_{\mathrm{final}} = 3265$ eV upon variation of the Bragg angle between 9.8° and 10.6°. The possibility to switch on or off specific lattice planes as reflectors turned out to be a valuable tool for disentangling the fine structure in the diffractograms. In view of such small Bragg angles a real-space description of the contrast reversal faces severe conceptual problems because of the necessity of long travelling distances of the photoelectrons. Moreover, the angular frequencies of the spherical harmonics must be very high in order to describe the observed rapid angular variations in the measured data. In turn, spherical harmonics up to high orders are required for a real-space scattering calculation, posing a severe numerical problem.

The advantage of the Bloch-wave model lies in the effective description of materials with perfect long-range order. The advantage of spherical-wave cluster calculations is their capability of treating non-3D-periodic systems like adsorbate structures. Both methods are thus equally powerful with complementary application scenarios.

The high-energy momentum microscope can record initial kinetic energies up to 8 keV and allows to perform full-field imaging of (k_x–k_y) photoelectron distributions with a large field of view in k-space (up to >22 Å^{-1} diameter). In order to observe the zone fine structure with high resolution we have chosen a k-field-of-view of 14 Å^{-1}, about twice the width of the principal Kikuchi band. Translated to real-space (angular) coordinates this corresponds to a polar angular range of only 0°–9°, being much less than typical angular ranges in previous XPD experiments. However, our k-resolution of 0.025 Å^{-1} is equivalent to an angular resolution of 0.034°, which is 1–2 orders of magnitude better than reported in previous work (all values for 7 keV kinetic energy).

A particularly intriguing advantage of the present approach is the possibility to combine high-resolution XPD, being sensitive on the geometric structure, with valence-band mapping, yielding the electronic structure. In the hard-x-ray regime the short photoelectron wavelength (<10% of the interatomic distances) 'amplifies' phase differences and turns hard-x-ray XPD into a very sensitive structural tool. Calculations for Si(001) revealed that changes of the lattice constant in the 1% range lead to clear changes in the fine structure near the zone axis (see figure 9 in [7]). This suggests possible applications of hXPD for element-resolved strain analysis in materials [50, 51]. Valence-band patterns are recorded at identical setting of the microscope [47] thus opening the path to a one-to-one correspondence of changes in the geometric and electronic structures, measured quasi simultaneously. Static and dynamic strain manipulation is emerging as a new avenue to tune and shape a material's electronic properties. Strong response of electronic structure upon elastic tuning has been found for certain symmetry-broken electronic quantum phases [52, 53].

A practical aspect is the possibility to align the orientation of the sample very fast using pronounced Kikuchi bands as in the present work. Thanks to the high intensity of the core-level signals, patterns like the series in figure 4 are visible with good contrast in real-time with frame rates of 1 Hz. The straight lines can then be used to adjust the electron optics avoiding image-field distortions at large *k*-field diameters. The size of the projected BZ is immediately visible in the Kikuchi patterns, providing a metric in *k*-space.

Because of its bulk sensitivity, hXPD momentum microscopy also offers a way to investigate temperature-dependent phase transitions in crystals, possibly with time-resolution in pump-probe experiments. For example, in combination with fs x-ray pulses available at Free Electron Lasers, site-specific photoemitters in compounds will be used as ultrafast internal electron probes for chemically-resolved crystallographic investigations.

We thus expect hXPD to be a powerful tool to investigate the dynamic interplay between the state of the crystal structure and the electronic states of a material, which is important both for fundamental solid state physics as well as for materials science applications.

Acknowledgments

Financial support by BMBF (projects 05K16UM1 and 05K16UM2) and Deutsche Forschungs-gemeinschaft (Transregio SFB 173 'Spin+X') is gratefully acknowledged.

ORCID iDs

O Fedchenko https://orcid.org/0000-0002-6159-7934
A Winkelmann https://orcid.org/0000-0002-6534-693X
D Vasilyev https://orcid.org/0000-0003-2870-3851

References

[1] Siegbahn K, Gelius U, Siegbahn H and Olson E 1970 Angular distribution of electrons in ESCA spectra from a single crystal *Phys. Scr.* **1** 272

[2] Fadley C S and Bergstrom S A L 1971 Angular distributions of photoelectrons from a metal single crystal *Phys. Lett.* A **35** 375

[3] Fadley C S 1987 Photoelectron diffraction *Phys. Scr.* **T17** 39
Fadley C S and Bachrach R Z (ed) 1992 *Synchrotron Radiation Research: Advances in Surface Science* vol 2 (New York: Plenum) p 421

[4] Fadley C S, Van Hove M A, Hussain Z and Kaduwela A P 1995 Photoelectron diffraction: new dimensions in space, time, and spin *J. Electron. Spectrosc. Relat. Phenom.* **75** 273

[5] Woodruff D P and Bradshaw A M 1994 Adsorbate structure determination on surfaces using photoelectron diffraction *Rep. Prog. Phys.* **57** 1029
Woodruff D P and Bradshaw A M 2002 *J. Electron Spectrosc. Relat. Phenom.* **126** 55–65

[6] Westphal C 2003 The study of the local atomic structure by means of x-ray photoelectron diffraction *Surf. Sci. Rep.* **50** 1–106

[7] Winkelmann A, Fadley C S and Garcia de Abajo F J 2008 High-energy photoelectron diffraction: model calculations and future possibilities *New J. Phys.* **10** 113002

[8] Fadley C S 2010 X-ray photoelectron spectroscopy: progress and perspectives *J. Electron Spectrosc. Relat. Phenom.* **2** 178–9

[9] Woodruff D P 2010 Surface structural information from photoelectron diffraction *J. Electron. Spectrosc. Relat. Phenom.* **186** 178–9

[10] Osterwalder J 2011 ed K Wandelt Photoelectron spectroscopy and diffraction *Handbook on Surface and Interface Science* (Weinheim: Wiley-VCH) vol 1, pp 151–214

[11] Kobayashi K, Kobata M, Masaaki I and Iwai H 2013 Development of a laboratory system hard x-ray photoelectron spectroscopy and its applications *J. Electron. Spectrosc. Relat. Phenom.* **190** 210–21

[12] Woicik J C (ed) 2016 *Hard X-ray Photoelectron Spectroscopy (HAXPES)* (*Springer Series in Surface Sciences* vol 59) (Berlin: Springer)

[13] Von Laue M 1948 *Materiewellen und ihre Interferenzen* (Leipzig: Akademische Verlagsgesellschaft Geest & Portig) p 392

[14] Goldberg S M, Baird R J, Kono S, Hall N F T and Fadley C S 1980 Explanation of XPS core-level angular distributions for single-crystal copper in terms of two-beam kikuchi-band theory *J. Electron Spectrosc.* **21** 1

[15] Trehan R, Fadley C S and Osterwalder J 1987 Single-scattering cluster description of substrate x-ray photoelectron diffraction and its relationship to kikuchi bands *J. Electron Spectrosc.* **42** 187

[16] Garcia de Abajo F J, Van Hove M A and Fadley C S 2001 Multiple scattering of electrons in solids and molecules: a cluster-model approach *Phys. Rev.* B **63** 075404
Fadley C S 2018 private communication

[17] Sinkovic B, Hermsmeier B and Fadley C S 1985 Observation of spin-polarized photoelectron diffraction *Phys. Rev. Lett.* **55** 1227

[18] Hermsmeier B, Osterwalder J, Friedmann D J and Fadley C S 1989 Evidence for a high-temperature short-range-magnetic-order transition in MnO(001 *Phys. Rev. Lett.* **62** 478

[19] Eastman D E, Donelon J J, Hien N C and Himpsel F J 1980 An ellipsoidal mirror display analyzer system for electron energy and angular measurements *Nucl. Instrum. Methods* **172** 327–36

[20] Daimon H 1988 New display-type analyzer for the energy and the angular distribution of charged particles *Rev. Sci. Instrum.* **59** 545–9

[21] Matsuda H *et al* 2014 Development of display-type ellipsoidal mesh analyzer: computational evaluation and experimental validation *J. Electron. Spectrosc. Relat. Phenom.* **195** 382–98

[22] Daimon H, Nakatani T, Imada S, Suga S, Kagoshima Y and Miyahara T 1993 Strong circular dichroism in photoelectron diffraction from nonchiral, nonmagnetic material–direct observation of rotational motion of electrons *Japan. J. Appl. Phys.* **32** L1480
Daimon H, Nakatani T, Imada S, Suga S, Kagoshima Y and Miyahara T 1995 *J. Electron Spectrosc. Relat. Phenom.* **76** 55

[23] Daimon H *et al* 1998 Direct structure analysis of W (110)-(1 × 1)-O by full solid-angle x-ray photoelectron diffraction with chemical-state resolution *Surf. Sci.* **408** 260–7

[24] Matsui F, Matsushita T and Daimon H 2014 Photoelectron structure factor and diffraction spectroscopy *J. Electron. Spectrosc. Relat. Phenom.* **195** 347–60

[25] Matsui F, Nishikawa H, Daimon H, Muntwiler M, Takizawa M, Namba H and Greber T 2018 The $4\pi k_z$ periodicity in photoemission from graphite *Phys. Rev.* B **97** 045430

[26] Osterwalder J, Fasel R, Stuck A, Aebi P and Schlapbach L 1994 Holographic interpretation of photoelectron diffraction *J. Electron. Spectrosc. Relat. Phenom.* **68** 1–18

[27] Katayama T, Yamamoto H, Koyama Y M, Kawazu S and Umeno M 1999 Kikuchi-band analysis of x-ray photoelectron diffraction fine structure of Si(100) by precise angle-resolved x-ray photoelectron spectroscopy *Japan. J. Appl. Phys.* **38** 1547–52

[28] Broekman L, Tadich A, Huwald E, Riley J, Leckey R, Seyller T, Emtsev K and Ley L 2005 First results from a second generation toroidal electron spectrometer *J. Electron. Spectrosc. Relat. Phenom.* **144–147** 1001–4

[29] Winkelmann A, Schröter B and Richter W 2004 Simulation of high energy photoelectron diffraction using many-beam dynamical kikuchi-band theory *Phys. Rev.* B **69** 245417

[30] DeWames R E and Hall W F 1968 A wave mechanical description of electron and positron emission from crystals *Acta Crystallogr.* A **24** 206–12

[31] Kirkland E J 2010 *Advanced Computing in Electron Microscopy* (New York: Springer)

[32] Rossouw C J, Miller P R, Josefsson T W and Allen L J 1994 Zone-axis back-scattered electron contrast for fast electrons *Phil. Mag.* A **70** 985–98

[33] Chung D D L 2002 Review graphite *J. Mater. Sci.* **37** 1475

[34] Humphreys C J 1979 The scattering of fast electrons by crystals *Rep. Prog. Phys.* **42** 1825–87

[35] Krasovskii E E 2003 The band structure theory of LEED and photoemission *Solid-State Photoemission and Related Methods* ed W Schattke and M A Hove (Wiley-VCH Verlag GmbH) (https://doi.org/10.1002/9783527602506.ch7)

[36] Henke B L, Gullikson E M and Davis J C 1993 X-Ray interactions: photoabsorption, scattering, transmission, and reflection at $E = 50–30{,}000$ eV, $Z = 1–92$ *At. Data Nucl. Data Tables* **54** 181

[37] Schlueter C *et al* 2018 New HAXPES applications at PETRA III *Synchrotron Radiat. News* **31** 29
Schlueter C *et al* 2019 *AIP Conf. Proc.* **2054** 040010

[38] Medjanik K *et al* 2019 Breakthrough in HAXPES performance combining full-field k-imaging with time-of-flight recording arXiv:1810.11366v1 [cond-mat.mtrl-sci]

[39] Medjanik K *et al* 2017 Direct 3D mapping of the fermi surface and Fermi velocity *Nat. Mater.* **16** 615

[40] Oelsner A, Rohmer M and Schneider C 2015 Time- and energy resolved photoemission electron microscopy-imaging of photoelectron time-of-flight analysis by means of pulsed excitations *J. Electron Spectrosc.* **178-179** 317

[41] Kikuchi S 1928 Diffraction of cathode rays by mica *Proc. Imperial Acad.* **4** 354–6

[42] Reimer L 1998 *Scanning Electron Microscopy—Physics of Image Formation and Micro-analysis* (Berlin: Springer)

[43] Williams D B and Carter C B 2009 *Transmission Electron Microscopy* (Berlin: Springer) ch 11 (https://doi.org/10.1007/978-0-387-76501-3)

[44] Zuo J M and Spence J C 2017 *Advanced Transmission Electron Microscopy* (Berlin: Springer) (https://doi.org/10.1007/978-1-4939-6607-3)

[45] Uyeda R 1936 On the inner potentials of graphite and prolybdenite *Proc. Phys.-Math. Soc. Japan. 3rd Ser.* **V20** 280

[46] Gray A X *et al* 2011 Probing bulk electronic structure with hard x-ray angle-resolved photoemission *Nat. Mater.* **10** 759

[47] Babenkov S *et al* 2019 High-accuracy bulk electronic bandmapping with eliminated diffraction effects using hard x-ray photoelectron momentum microscopy *Commun. Phys.* **2** 107

[48] Veneklassen R 1991 Design of a spectroscopic low-energy electron microscope *Ultramicroscopy* **36** 76

[49] Bauer E 1998 LEEM basics *Surf. Rev. and Lett.* **05** 1275–86

[50] Wilkinson A J and Britton T B 2012 Strains, planes, and EBSD in materials science *Mater. Today* **15** 366

[51] Ojima M, Adachi Y, Suzuki S and Yo T 2011 Stress partitioning behavior in an fcc alloy evaluated by the *in situ*/ex situ EBSD-Wilkinson method *Acta Mater.* **V59** 4177

[52] Kim H-H *et al* 2018 Uniaxial pressure control of competing orders in a high-temperature superconductor *Science* **362** 1040

[53] Song G, Borisov V, Meier W R, Xu M, Dusoe K J, Sypek J T, Valentí R, Canfield P C and Lee S-W 2019 Ultrahigh elastically compressible and strain-engineerable intermetallic compounds under uniaxial mechanical loading *APL Mater.* **7** 061104